

A short-orbit spectrometer for low-energy pion detection in electroproduction experiments at MAMI

D. Baumann^a, M. Ding^a, I. Friščić^{b,1,*}, R. Böhm^a, D. Bosnar^b, M. O. Distler^a, H. Merkel^a, U. Müller^a, Th. Walcher^a, M. Wendel^a

^a*Institut für Kernphysik, Johannes Gutenberg-Universität, 55099 Mainz, Germany*

^b*Department of Physics, Faculty of Science, University of Zagreb, Bijenička c. 32, 10000 Zagreb, Croatia*

Abstract

A new Short-Orbit Spectrometer (SOS) has been constructed and installed within the experimental facility of the A1 collaboration at Mainz Microtron (MAMI), with the goal to detect low-energy pions. It is equipped with a Browne-Buechner magnet and a detector system consisting of two helium-ethane based drift chambers and a scintillator telescope made of five layers. The detector system allows detection of pions in the momentum range of 50 – 147 MeV/c, which corresponds to 8.7 – 63 MeV kinetic energy. The spectrometer can be placed at a distance range of 54 – 66 cm from the target center. Two collimators are available for the measurements, one having 1.8 msr aperture and the other having 7 msr aperture. The Short-Orbit Spectrometer has been successfully calibrated and used in coincidence measurements together with the standard magnetic spectrometers of the A1 collaboration.

Keywords: Short-orbit spectrometer, Low-energy pions, Electroproduction experiments

PACS: 29.30.-h (Spectrometers for nuclear physics), 25.30.Fj (Inelastic electron scattering in nuclear reactions)

1. Introduction

The $p(e, e'\pi^+)n$ reaction, measured with high precision close to threshold, provides a great tool for studying the axial and the pseudoscalar form factor [1, 2]. One of the experimental setups capable performing such experiments is the high resolution spectrometer setup of the A1 collaboration [3] using the electron accelerator Mainz Microtron (MAMI) [4].

The A1 spectrometer setup consists of two large acceptance (28 msr) spectrometers (A and C) having a quadrupole-sextupole-dipole-dipole magnet configuration and a third spectrometer (B), which is based on one clamshell dipole. This spectrometer is slimmer and can reach scattering angles down to 7° , but this comes at the cost of smaller acceptance (5.6 msr). Each spectrometer is equipped with a particle tracking system based on 4 vertical drift chamber layers and a particle identification system based on scintillating paddles and Čerenkov detectors. If needed, these can be replaced with other detector configurations. The spectrometers can be rotated around the target chamber in the center and they can be operated in a single, double, and triple coincidence mode. Looking along the beam direction, spectrometers A and C are placed on the left and right side of the beam pipe, respectively. Spectrometer B can be moved to either side of the beam pipe; in standard configuration it is placed on the right side. All three spectrometers have a relative momentum resolution $\leq 10^{-4}$ and are used in different electron scattering experiments for detection of charged

particles having momenta up to 735 MeV/c in A, 870 MeV/c in B and 551 MeV/c in C. For unstable particles the use of spectrometers is limited to high momenta, which allow the particles to reach the detector system before they decay.

The pion is an unstable particle having a lifetime of 26.033 ns, which dominantly decays into a muon and a muon neutrino [5]. Close to the reaction threshold it will have low kinetic energy. Since the distance from target to standard detector system inside the spectrometers of the A1 collaboration is of the order of 10 m, most of the low energy pions will decay before they reach the detectors. The measurement time needed for collection of statistically relevant data would be prolonged. Moreover, a fraction of muons will be created close to the direction of pions and will be also detected. Such muons cannot be distinguished from the pions and they are a major source of systematic error. The influence of these two problems can be reduced simultaneously by decreasing the distance between target and detector system. Significantly more pions will now survive to the detector system for the same kinetic energy, but the data still has to be corrected for pion decay. At the same time, muon contamination of the data will be reduced, so that it is feasible to determine it from a simulation and correct for it.

Therefore, a new short orbit spectrometer (SOS) was constructed specifically for detection of low energy pions. The $^{12}\text{C}(e, e'\pi^+)^{11}\text{B}$ reaction was used for calibration of the SOS. As the first physics experiment, the $p(e, e'\pi^+)n$ reaction was evaluated, which at the same time allowed to test the performance of the SOS in detection of low energy pions.

Section 2 of this paper describes the magnet, detector system and electronics of the SOS. In section 3 the measurement used for calibration of the SOS is discussed. Section 4 deals with a measurement of the $p(e, e'\pi^+)n$ reaction. A summary and a

*Corresponding author, Email: friscic@mit.edu

¹Present address: MIT-LNS, Cambridge MA, 02139, USA

²This paper comprises parts of the doctoral theses of D. Baumann, M. Ding and I. Friščić.

conclusion are done in section 5.

2. Short-orbit spectrometer outline

2.1. Construction objectives

The objectives of the spectrometer's construction arise from the following experimental considerations:

1. In order to minimise the above mentioned loss due to pion decay and at the same time reduce muonic background, the spectrometer has a flight path of only 1.6 m from target to detector system.
2. Good missing mass resolution, e.g. for the neutron in the $p(e, e'\pi^+)n$ reaction, is desirable, because it will help to identify the reaction's final state, as well as to reduce background noise. For this, the SOS must be able to detect low energy pions with good spatial and momentum resolution. This requires focusing at least in the dispersive plane of the spectrometer magnet as well as a position sensitive detector. The reaction vertex in the target can be determined independently, using information of the beam position and data from the electron spectrometer.
3. The detector needs to have a small effective mass thickness to minimise multiple scattering and energy loss of particles down to low energies. Therefore, a drift chamber with a helium based counting gas was chosen as tracking detector.
4. For further reduction of charged particle background, the detector should allow particle identification, i.e. discrimination of pions from protons, electrons or positrons. This is achieved by a scintillator range telescope. In addition, time of flight is measured. But in the pion arm this is of limited use due to the short path length. Use of an aerogel or plastic Čerenkov counter was rejected because it would offer no advantage over the range telescope in the intended momentum range.
5. Solid angle acceptance should be reasonably high. However, short path length was deemed more important for the considered experiments. Therefore, the spectrometer does not feature additional focusing by a quadrupole, which limits its solid angle to at most 7 msr. Furthermore, measurements with an extended target, like a liquid hydrogen target cell with 2 cm diameter, should be possible.
6. The spectrometer should be movable over a wide angle range in order to maximise the available kinematics, e.g. the variation range of the polarisation parameter ϵ [2]. This implies small relative angles to the beamline, as well as to the other spectrometers.

2.2. Magnet

The SOS, see Fig. 1 and 2, comprises a Browne-Buechner type dipole magnet [6] having circular pole pieces with a radius of 350 mm. The magnet from the previous Mainz pion spectrometer was available and could be used with some modifications. See ref. [7] for a detailed description of the magnet.

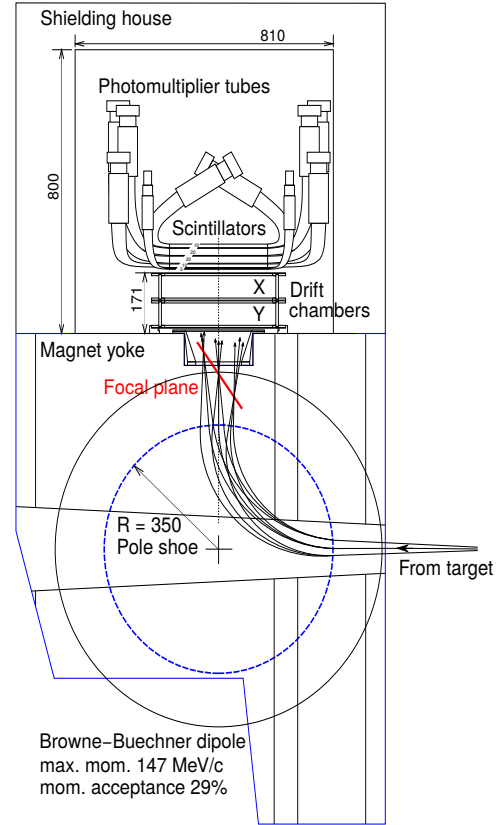


Figure 1: (colour online) Schematic of SOS and the detector system. All measures are in millimeters. The target is positioned approx. 1.1 m to the right and aligned with the central cross.

The magnet has three focal planes. Two of them correspond to $\pm 90^\circ$ deflection of the reference trajectory and can be used for momenta less than 150 MeV/c. They allow detection of positive and negative charged particles simultaneously. The third focal plane is located in the rear lower part of the SOS. It can be used for particles having momenta in range of 150 – 300 MeV/c. At the present time, only the upper focal plane is equipped with a detector system. The spectrometer was designed to accept particles with momenta up to 147 MeV/c for a magnetic field of 1.4 T. The momentum acceptance ranges from -13% to 16% . The SOS is mounted on the support of spectrometer B, which allows adjustment of the spectrometer angle with a 0.01° resolution. During the measurement with the SOS, spectrometer B cannot be used.

The shape of the magnet yoke was modified by milling in order to allow for a smaller angle relative to the exit beamline, thereby maximizing the ϵ range. Also the smallest possible angle relative to the other spectrometers was diminished. Before the milling, the influence of the yoke's shape on the homogeneity of the magnetic field was investigated via computer simulation. After the reassembly of the magnet the homogeneity of the magnetic field was measured for several strengths of the field. No significant changes were observed before and after the modification. For a distance of 66 cm between SOS and target center the modification of the yoke's shape allows the minimum

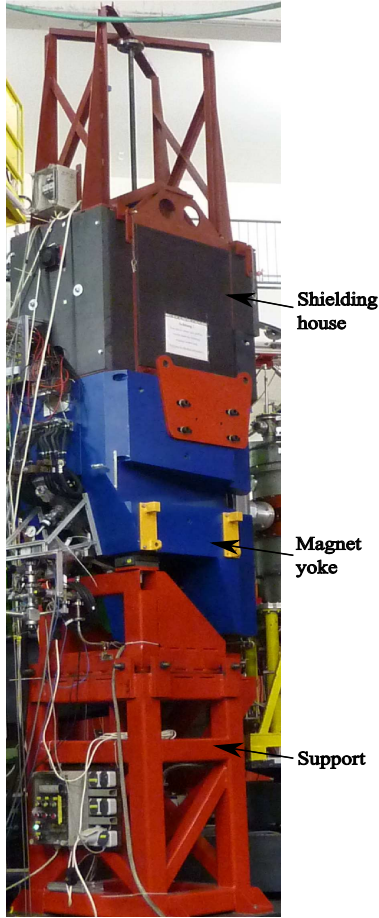


Figure 2: (colour online) Photo of the SOS. The stand of the SOS is mounted on the support of spectrometer B. It carries the magnet yoke and it allows fine alignment of the yoke with respect to the target center. Above the yoke is the shielding house containing the detector system, which can be accessed for maintenance by lifting the sides of the shielding house.

relative angle between SOS and spectrometers A and C of 55° . The minimum forward angle is 15.4° . At a distance of 54 cm the minimum forward angle is 22° .

It is possible to directly connect the vacuum system of the magnet and the scattering chamber. In this way the need for two additional foils, as well as the air gap between the two foils can be avoided. The accessible angles are limited then, due to several discrete openings of the scattering chamber. A change of angular position requires uncoupling of the SOS from the scattering chamber. This includes a breach in the vacuum system. In this work due to running time and angle limitations, the scattering chamber and the magnet vacuum were not directly connected.

The vacuum system of the magnet ends with a tapered flange, sealed with a $50\ \mu\text{m}$ thick polyimide foil ("Kapton"). The bending of the Kapton foil caused by the vacuum stress leads to formation of an air pocket in the created free space. This volume is flushed with helium gas for further reduction of multiple scattering. The upper cover, just below the drift chambers, is made out of $6\ \mu\text{m}$ aramid foil having only small helium permeability.

2.3. Collimators

Altogether, the SOS is equipped with three different collimators. Two are meant to be used in experiments and the third one is a "sieve" collimator for determination of transfer matrices. The collimators were developed for the measurements with an extended target. The size of the collimator's aperture was optimized with respect to the distance from target, so that the accepted solid angle was maximized and the amount of internal scattered particles was minimized. However, since a Browne-Buechner magnet is only single-focusing in the dispersive plane, the maximum achievable solid angle is limited.

One collimator was developed for experiments in which the SOS will be placed at 66 cm from the target center, while a target cell with diameter of 2 cm will be used. To ensure that no particles from the target cell will hit the pole shoes, the solid angles of this collimator was limited to 1.8 msr [8].

For a certain angle range between the limiting values (described above) the SOS can be also mounted closer to the target. On one hand, a larger solid angle provides a reduction of measurement time. On the other hand, due to shorter orbits a smaller number of pions will decay into muons. The distance of 54 cm was found to be an optimal value. But for this distance it was not possible to design a collimator, which ensures that no particles from the target hit the magnet poles. Due to this fact the collimator aperture of 7 msr is reduced to approximately 4 msr [8]. Particles scattered on the magnet poles have to be taken into account during the analysis.

The third collimator is a sieve collimator with an irregular array of holes. It is used for a (inverse) transfer matrix determination.

All collimators are made of the same tungsten-copper alloy ("Densimet 18" by Plansee). The thickness of the sieve collimator and the other two collimators is 5 mm and 45 mm, respectively.

2.4. Drift chambers

Since a part of the magnet's focal plane is situated inside the influence of fringe fields, the tracking detector has to be placed outside the focal plane. Therefore, the tracking detector was realized by using two volume type drift chambers, see Fig. 3.

The effective thickness was kept small by reducing the number of foils to three: two outer and one shared. The shared foil was grounded in order to separate the electric field configurations of upper and lower chamber. Furthermore, due to its larger radiation length than argon, helium was chosen as a counting gas and ethane as a quencher. During the measurement the chambers are operated with 1:1 gas ratio, ensuring in this way almost constant drift velocity for a wide range around the working voltage [9]. Aging of the wires is inhibited by enriching the gas mixture with ethanol before it enters the chambers. Thickness and radiation length of the employed materials are given in Table 1.

The chamber frame is made of epoxy reinforced with fibreglass (Stesalit AG, CH-4234 Zullwil). The wires are tensioned and then held in place by crimping them in feedthrough ferrules (Ferrini S.A., CH-6596 Gordola). These have an inner bore of

Table 1: Contributions to effective thickness of SOS tracking detector, x is thickness of a layer and X_0 is radiation length of the employed material.

Material	x	X_0 (cm)	$x/(10^{-6}X_0)$	Comment
He + C ₂ H ₆	152 mm	63900	238	Counting gas
PET	(4+4+12) μ m	28.7	69.7	Chamber foils (CF)
Al	2·(10+10+40) nm	8.9	1.35	Coating on the CF
Al	367 nm	8.9	4.1	Potential wires (averaged)
Drift chambers			313	Sum for the chambers
Polyimid	50 μ m	28.6	175	Vacuum exit
Aramid	6 μ m	28.6	21.0	He-flange foil
Helium	20 mm	568000	3.5	Gap below the chamber
Rest			277	Everything outside the chamber
Altogether			590	From target to scintillator

80 μ m or 150 μ m in order to center the signal and potential wires, respectively. The ferrules also provide electrical contact for the wires. Additional details are listed in Table 2.

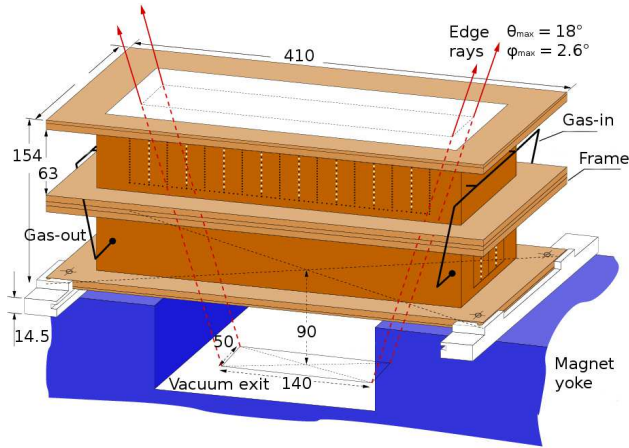


Figure 3: (colour online) The SOS drift chambers in a build-in position. The bottom chamber is used for reconstruction of non-dispersive coordinates, and the upper chamber for dispersive coordinates. Positions of the signal wires are marked with white points. Edge rays were determined with help of RAYTRACE simulation.

Fig. 4 exemplarily shows a single SOS drift cell. Each drift cell is made of eight vertically arranged signal wires, which are alternatingly shifted by 100 μ m with respect to the center of the cell. In the trajectory reconstruction procedure the shifts are taken into account to determine at which side the particle has passed the signal wire – so-called left-right decision. The signal wires are grounded by the preamplifier. The potential wires (cathode wires) at the edges of the drift cells are set to a high negative voltage, typically -5400 V. In order to obtain drift cells with well defined borders and to mutually suppress the cross talk between neighboring drift cells, potential wires closest to the signal wires are set to an intermediate voltage by a voltage degrader. The best averaged single wire efficiency of 95% was achieved, when the ratio of the cathode wire and intermediate voltage was 4 : 1 [10]. In order to assure that the

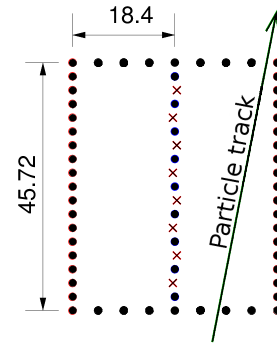


Figure 4: (colour online) Lateral profile of a single SOS drift cell. Circles represent potential wires and crosses represent signal wires, signal wires, which are staggered left and right by 100 μ m. In order to make the signal wire staggering visible on this figure, it is exaggerated.

boundary drift cells also have a proper geometry of the electric field, only potential wires at the edges of the signal wires vertical arrangement are grounded.

Table 2: Properties of the SOS drift chambers.

Outer dimensions	410 x 210 x 156 mm ³
Active surface	294.4 x 73.6 mm ²
Wire drift cell length x width	18.4 x 5.08 mm ²
Signal wires horizontal offset	± 100 μ m
Number of signal wires	64/16 (X-/Y-chamber)
Number of potential wires	355/103 (X-/Y-chamber)
Signal wires:	$\varnothing 15$ μ m Au-coated tungsten-rhenium
Potential wires:	$\varnothing 80$ μ m Ag-coated aluminium
Gas:	50% helium + 50% ethan

The Y-chamber with two drift cells is the first chamber above the magnet. It measures the non-dispersive coordinate and angle (y_{ch}, ϕ_{ch}). The second chamber consisting of eight cells is the X-chamber. The wires of the X-chamber are perpendicular to the wires of the Y-chamber and, therefore, it measures the dispersive coordinate and angle (x_{ch}, θ_{ch}). Particles enter the

X-chamber after the Y-chamber and due to multiple scattering, resolution of the X-chamber will always be lower relative to the Y-chamber. The priority to Y-chamber was given to provide better discrimination of particles which may be scattered from the magnet edges and to allow better estimation of particle energy loss inside a target.

The individual signal wires are connected to preamplifier and discriminator cards (LeCroy 2735 DC) which are mounted to the chamber's frame. The signals are then digitized by TDCs (TDC2001) with $2 \mu\text{s}$ measuring range and 250 ps time resolution.

2.5. Scintillator range telescope

The SOS range telescope has two tasks. First, it gives a timing signal for the trigger and common stop for the drift chambers. Second, it allows particle identification by range information and particle energy deposition in a certain scintillator layer, see Fig. 5. The range telescope is composed of five scintillator layers. Scintillators are made of Bicron BC 408 type plastic. Each scintillator has the same width of 80 mm and length of 300 mm, but they differ in thickness. From bottom to top, the scintillator's thickness are 3, 10, 20, 20 and 10 mm, respectively, see Fig. 5. The scintillators are equipped with PMTs at both lateral ends. Read-out is performed in coincidence for background suppression. The thinnest scintillator is read-out by Philips XP 2910 PMTs and all other scintillators by Philips XP 2262B PMTs.

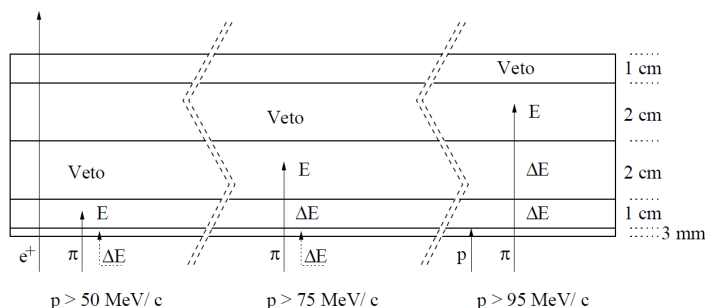


Figure 5: Illustration of the particle identification in the scintillator range telescope. Protons are stopped in the bottom scintillator, positrons pass through all layers, pions are stopped in a certain layer depending on their momentum. In order to enter the second scintillator the pions need to have momenta larger than 50 MeV/c and so on [8].

So-called "twisted-strip" Plexiglas light guides are used to connect PMTs and scintillators. This type of light guide was produced by first bending the individual strips to the desired radius and then gluing the strips together. Individual strips have to be of same length, to ensure simultaneous arrival of the light to PMT. However, due to limitations by critical bending radii, as well as the compact build of the shielding house, same length for all strips was not feasible. Nonetheless, the length difference of the strips was still acceptable and was less than 2 cm. The optical coupling between scintillator and light guide was realized by using optical cement Bicron BC-600. For optical coupling

between the light guide and PMT, two-component silicon rubber (Wacker Elastosil RT 601) was used. This glue allows easy detachment of a PMT if it needs to be replaced. The PMTs are placed on an aluminium fixture and shielded against magnetic fields using μ -metal.

2.6. Shielding house

The detectors are located inside a shielding house which consists of an outer 5 cm layer of borated polyethylene to absorb neutrons and an inner 10 cm layer of lead to shield electromagnetic background. This specific shielding configuration was chosen in order to maximise the available space inside the shielding house, for better accommodation and easier mounting of the detector system, while still retaining the best possible shielding effect. Therefore, an originally planned 5 cm layer of normal, unborated polyethylene was omitted in the final design [11].

Since the drift chambers are not leak-proof, some amount of helium could diffuse into PMTs and damage them. To prevent this, the shielding house is divided with plastic plates in an upper (scintillator) and lower (drift chamber) part. Additionally, the chamber part is kept under-pressurized by a ventilator at the end of an exhaust tube, which connects the chamber part and the rear wall of the shielding house.

2.7. Trigger and data acquisition

In order to achieve high event rates, the SOS is equipped with independent electronics and a trigger logic system. Each of the two PMTs of the five scintillators provides an analog signal which is then split, one half being sent to an ADC (LeCroy 2249A) for charge digitization, the other half being converted by a discriminator into a logical signal.

A minimal condition for generation of a trigger signal requires that both PMTs of a single scintillator layer produce signals larger than a specified threshold. This minimal trigger condition can be extended by requesting different logical conditions between trigger signals of individual layers, for example, by requiring generation of trigger signals in two or more scintillators, or by using one or more scintillator layers as veto detectors. This is achieved by using a programmable look-up unit (LeCroy PLU 4508) which also allows an on-line change of trigger conditions. An additional input of the PLU is used to inhibit triggers during data readout.

3. Calibration of SOS with quasielastic proton knockout from ^{12}C

Usually, calibration of a magnetic spectrometer is performed using the electrons from the elastic scattering of a selected nucleus, since in this case the momentum of a scattered electron is only dependent on the scattering angle. Because of the maximum momentum accepted by the SOS (147 MeV/c), the elastic scattered electron produced by the minimum electron beam energy of 180 MeV, provided by MAMI, does not comply with SOS requirements. Hence, another reaction has to be used for the calibration of the SOS. The choice for a suitable reaction

was guided by the fact that the scattered electron has to lose enough momentum in order to comply with the SOS's momentum acceptance. The quasielastic electron scattering from a ^{12}C nucleus with proton knockout meets these demands: protons inside a ^{12}C nucleus are not static, they move (Fermi-motion) having a momentum distribution with a maximum at 100 MeV/c [12, 13]. If the remaining ^{11}B nucleus is determined to be in the ground state, it is certain that the outgoing proton, which is detected in spectrometer A, originates from the $1p_{3/2}$ level of the ^{12}C nucleus, Fig. 6.

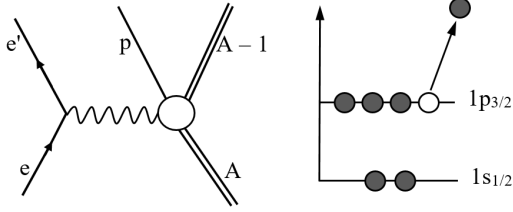


Figure 6: On the left: illustration of the quasielastic electron scattering on a nucleus having a mass number A with a proton knockout. On the right: in the case of ^{12}C , knowing that the remaining ^{11}B is in the ground state ensures that the proton was knocked out of the p -shell.

Therefore, the SOS calibration measurement has been performed using a ^{12}C foil with area density of 30 mg/cm^2 as target. Table 3 summarizes the kinematical settings used for the calibration of the SOS. For setting 1 from table 3, the energy transfer is $\omega = 55 \text{ MeV}$, which is in the case of the quasielastic proton knockout from ^{12}C divided between the separation energy $E_{sep} = (m_p + m_{^{11}\text{B}} - m_{^{12}\text{C}})c^2$, excitation energy of the residual ^{11}B nucleus E_x , kinetic energies of the proton E_p and the residual ^{11}B nucleus $E_{^{11}\text{B}}$:

$$\omega = E - E' = E_{sep} + E_x + E_p + E_{^{11}\text{B}} \quad (1)$$

From equation (1) and the measured proton momentum it is now possible to determine the momentum of the scattered electron and perform calibration of the SOS. Four-momentum based calculation of recoil energy leads to an exact expression for the energy of the scattered electron [9]. The idea is to define a four-momentum $\kappa = p_e + p_{^{12}\text{C}} - p_p$, which can be easily obtained by the measured quantities. Using the momentum conservation law one obtains:

$$p_{^{11}\text{B}} = \kappa - p'_e \quad (2)$$

Taking the square of equation (2) and neglecting electron mass one has:

$$E'_{calc} = \frac{\kappa^2 - m_{^{11}\text{B}}^2}{2\kappa \cdot \hat{\eta}} \quad (3)$$

where the spatial part of the unit vector $\hat{\eta} = (1, \sin\theta_e, 0, \cos\theta_e)$ points in the direction of the scattered electron. Equation (3) depends on the electron scattering angle θ_e . Using the sieve collimator the variation of θ_e can be kept small enough to use equation (3) for the calibration of the SOS.

The scattered electron in the SOS and the knockout proton in spectrometer A were detected in coincidence between those

Table 3: Central kinematical parameters for the calibration of the SOS: E is the beam energy, p_A and θ_A are central momentum and angle of spectrometer A, p_{SOS} and θ_{SOS} are central momentum and angle of SOS, respectively.

Setting	E (MeV)	p_A (MeV/c)	θ_A ($^\circ$)	p_{SOS} (MeV/c)	θ_{SOS} ($^\circ$)
1	180	265	43.0	125	60.0
2	180	265	43.0	115	60.0
3	180	290	43.0	115	60.0

two spectrometers. The trigger in spectrometer A was formed by requiring a signal in both scintillator planes (ΔE and ToF), but the timing information was defined only by the ToF plane. Coincidence time was corrected for the path length of the particle only in spectrometer A. After this correction, a coincidence peak with a time resolution of 1.98 ns FWHM was obtained, which was sufficient to determine the transfer matrices for the SOS. A cut of $-2 \text{ ns} \leq T_{A-SOS} \leq 2 \text{ ns}$ was used to select true coincidence events.

The background of minimum ionizing particles was suppressed by imposing an appropriate cut on the deposited energy in the ΔE scintillator plane. For further reduction of background additional cuts were applied on the angular acceptance of spectrometer A ($|\theta_0| \leq 5.1^\circ$ and $|\phi_0| \leq 0.6^\circ$).

Using the measured four-momentum of the proton (E_p, \vec{p}_p) and transfer four-momentum defined by the electron arm (ω, \vec{q}) it is possible to calculate the missing mass of the unobserved ^{11}B nucleus m_{miss} and extract its excitation spectrum E_x :

$$E_x = m_{miss} - m_{^{11}\text{B}} = \sqrt{(\omega + m_{^{12}\text{C}} - E_p)^2 - (\vec{q} - \vec{p}_p)^2} - m_{^{11}\text{B}} \quad (4)$$

Fig. 7 shows the excitation spectrum of the ^{11}B nucleus for kinematical setting 2 from table 3. The spectrum is dominated by the ground state having an experimental width of 1.41 MeV/c² FWHM.

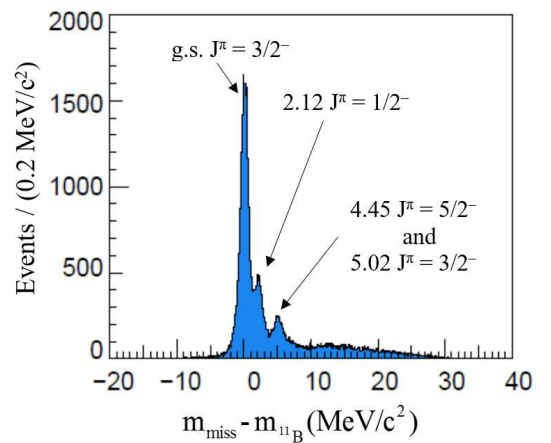


Figure 7: (colour online) The ^{11}B excitation energy spectrum of the $^{12}\text{C}(e, e'p)^{11}\text{B}$ reaction (Setting 2). The peak centered at 0 MeV/c² belongs to the ground state and has a width of 1.41 MeV/c² FWHM. The second peak is the first excited state at 2.12 MeV and the third peak is caused by higher excited states at 4.45 MeV and 5.02 MeV [14].

3.1. Momentum resolution

In order to estimate the momentum resolution of the SOS, the following assumptions were made. For setting 2, protons (265 MeV/c) have a kinetic energy of 37 MeV and according to the Bethe-Bloch equation [5] they lose 0.43 MeV of energy for a 30 mg/cm² ¹²C target transit. Since protons created deeper inside the target will have less energy loss, the value of 0.43 MeV will be used as an upper limit for the estimate of the proton's energy uncertainty ΔE_p . This can also be expressed as the proton's momentum uncertainty $\Delta|\vec{p}_p|$:

$$\Delta|\vec{p}_p| = \frac{E_p}{|\vec{p}_p|} \Delta E_p \approx 3.676 \Delta E_p \quad (5)$$

The average energy loss of the electron beam ($E = 180$ MeV) inside the ¹²C target is up to 57.6 keV and up to 58.4 keV for scattered electrons ($E' \approx 115$ MeV). In order to simplify calculations, the electron's momentum uncertainty is assumed to come exclusively from the beam's energy loss ($\Delta E \approx 58$ keV). Using equation (4) the uncertainty of the excitation spectrum ΔE_x can be easily calculated:

$$\begin{aligned} (\Delta E_x)^2 &= \left(\frac{\partial E_x}{\partial E} \Delta E \right)^2 + \left(\frac{\partial E_x}{\partial E'} \Delta E' \right)^2 + \left(\frac{\partial E_x}{\partial |\vec{p}_p|} \Delta |\vec{p}_p| \right)^2 \\ &\approx 1.02 (\Delta E)^2 + 1.02 (\Delta E')^2 + 0.0795 (\Delta |\vec{p}_p|)^2 \\ &\approx 1.02 (\Delta E)^2 + 1.02 (\Delta E')^2 + 1.074 (\Delta E_p)^2 \end{aligned} \quad (6)$$

The last line in equation 6 was obtained by using equation 5. Finally, an error-less reconstruction of the proton momentum in spectrometer A is assumed. For $\Delta E_x = 1.41$ MeV, $\Delta E_p = 0.43$ MeV and $\Delta E = 0.058$ MeV the upper limit of SOS's momentum resolution is estimated as $\Delta E' \lesssim 1.31$ MeV.

Expressed in terms of relative momentum resolution this amounts to $1.31/115 \approx 1.14\%$. This relatively large value results from the missing momentum resolution of the participating proton. How much multiple scattering of low energy protons influences the momentum resolution of spectrometer A was not investigated in the framework of this work, since it was not essential for the creation of the transfer matrices.

If the full momentum acceptance range of the SOS is reduced, the corresponding width of the ground state peak is reduced to 1.2 MeV/c² FWHM. The same effect is also observed if one reduces the momentum acceptance range of spectrometer A. This is to be expected, since the acceptance ranges of both spectrometers are correlated with each other via the quasielastic proton knockout process. Consequently, it looks like momentum determination in a central region works better than towards the edges of the momentum acceptance. Or in other words, the magnet optics are not free of aberration.

3.2. Angular resolution at target

The angular resolution at target was estimated using the procedure described in [15]. Individual holes of the sieve collimator are described with the aperture angle θ_ϵ . For a distance of 66 cm from target to collimator, the aperture angle of the collimator's 2 mm and 3 mm holes are 3.03 mrad and 4.55 mrad, respectively.

If the distributions of dispersive angle θ_0 and non-dispersive angle ϕ_0 have corresponding widths $\Delta\theta_0$ and $\Delta\phi_0$, the following upper estimations of angle resolutions can be made:

$$\begin{aligned} \sigma_{\theta_0} &\leq \sqrt{(\Delta\theta_0)^2 - \theta_\epsilon^2} \\ \sigma_{\phi_0} &\leq \sqrt{(\Delta\phi_0)^2 - \theta_\epsilon^2} \end{aligned} \quad (7)$$

The data for estimation of angular resolution was selected by the cut around the nominal hole positions as follows:

$$(\theta_0 - \theta_0^{nom})^2 + 4 \cdot (\phi_0 - \phi_0^{nom})^2 < (0.6^\circ)^2 \quad (8)$$

Relative to the hole center used cuts were $\pm 0.6^\circ$ for θ and $\pm 0.3^\circ$ for ϕ . The FWHM values of the angle distributions, averaged over all kinematical settings and number of holes, were $\Delta\theta_0 = 11.6$ mrad (3 mm holes) and 11.0 mrad (2 mm holes). Finally, after averaging over hole sizes a resolution value of $\sigma_{\theta_0} = 10.6$ mrad was obtained for the dispersive angle at the target.

For the non-dispersive angle the averaged FWHM value of $\Delta\phi_0 = 3.3$ mrad was only determined for holes having 2 mm diameter (equation (7) could not be used for 3 mm holes, since the uncertainty was smaller than the aperture angle). A resolution value of $\sigma_{\phi_0} = 1.3$ mrad was obtained for the non-dispersive angle at the target.

RAYTRACE [16, 17] simulations of particle trajectories having $\theta_0 > 0$ predict a smaller value of σ_{ϕ_0} compared to those having $\theta_0 < 0$ [11]. This can be clearly observed in Fig. 8: with increasing of θ_0 , distributions of the individual holes get narrower. Described effect can be explained that the particles having positive θ_0 (going down inside the SOS) are slightly focused in the non-dispersive direction by the magnet's fringe fields and, therefore, angular acceptance has a trapezoidal shape.

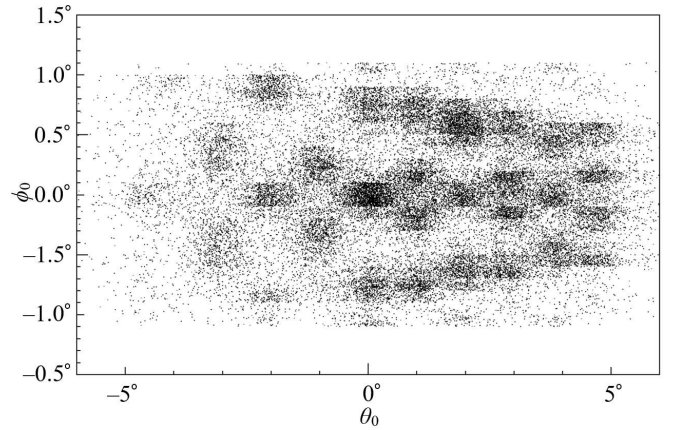


Figure 8: Calculated target coordinates θ_0 and ϕ_0 for the electron momentum of 125 MeV/c and cuts on coincidence peak $|T_{A-SOS}| < 2$ ns, on ¹¹B ground state $|E_x| < 2.5$ MeV/c², on wire multiplicity > 5 in both chambers and on SOS momentum acceptance $-13\% < \delta p_0 < 16\%$. Measurement was performed with sieve collimator.

3.3. Experimental determination of transfer matrix

The full coverage of aperture edges of the two above mentioned collimators is achieved by placing the sieve collimator at

two different positions. In those two positions none of the holes overlap with each other, so that the number of coordinates used in determination of the transfer matrix is doubled.

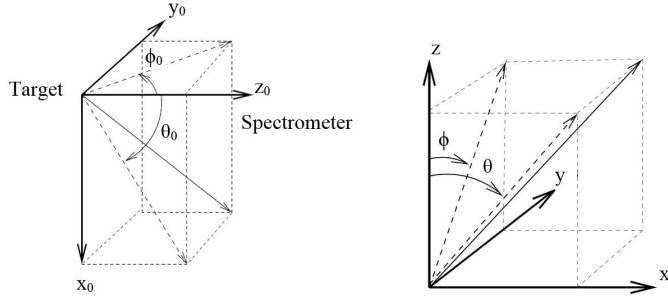


Figure 9: Definition of target coordinate system (left) and chamber coordinate system (right), from [15].

In the target coordinate system (Fig. 9) positions of the holes are defined by dispersive angle θ_0 and non-dispersive angle ϕ_0 . Additionally, in the dispersive xz -plane we also have the difference from the central momentum $\delta p_0 = \Delta p/p$ and in the non-dispersive yz -plane we have the vertex coordinate y_0 in the direction of the beam. By using drift chamber measurements, the position of each hole can be determined and mapped in terms of the chamber coordinates $(\theta_{ch}, x_{ch}, \phi_{ch}, y_{ch})$. Now it is possible to write the dispersive target coordinates θ_0 and δp_0 as functions of the dispersive chamber coordinates (θ_{ch}, x_{ch}) , as well as the non-dispersive target coordinates ϕ_0 and y_0 as functions of (ϕ_{ch}, y_{ch}) . The coefficients of these functions form the transfer matrix. In addition, we have the path length l , which is needed for correction of coincidence time.

An example of transfer matrix coefficients and corresponding functions obtained for the kinematical setting 1 and cuts on coincidence peak $|T_{A-SOS}| < 2$ ns, on the ^{11}B ground state $|E_x| < 2.5$ MeV/ c^2 , on wire multiplicity > 5 in X- and Y-chamber, and on SOS momentum acceptance $-13\% < \delta p_0 < 16\%$ is:

$$\begin{aligned} \delta p_0 &= 1.85 \cdot x_{ch} - 0.018 \cdot \theta_{ch} + 0.0014 \cdot x_{ch} \cdot \theta_{ch} \\ \theta_0 &= 8.512 \cdot x_{ch} - 0.520 \cdot \theta_{ch} \\ y_0 &= 0.383 \cdot y_{ch} - 0.045 \cdot \phi_{ch} \\ \phi_0 &= 5.011 \cdot y_{ch} + 0.037 \cdot \phi_{ch} \\ l &= 163 \text{ cm} \end{aligned} \quad (9)$$

where δp_0 is expressed in percentage, all angles are expressed in mrad and all lengths in cm. Angles at target θ_0 and ϕ_0 reconstructed using this matrix can be seen in Fig. 8.

The obtained transfer matrices are not suitable for reconstruction of the target coordinate y_0 , because they have been produced by using only one carbon foil as target. In order to be sensitive to y_0 , calibration of the SOS has to be performed with a stack of carbon foils with well defined distances between the individual foils.

4. Test measurement of the $p(e, e'\pi^+)n$ reaction

The $p(e, e'\pi^+)n$ reaction was measured at an invariant mass of $W = 1084.3$ MeV (~ 5 MeV above threshold) and a four-

momentum transfer of $Q^2 = 0.078$ (GeV/ c) 2 . Other parameters of the measured kinematical setting are summarized in table 4. Liquid hydrogen inside a cylindrical cell was used as target. The cell, 2 cm in diameter, was made of a 50 μm Havar foil as boundary. Density fluctuations inside the liquid hydrogen were avoided by recirculation of the liquid hydrogen and by rastering the electron beam in transverse directions.

Table 4: Central kinematical parameters for the $p(e, e'\pi^+)n$ reaction: ϵ is the transversal polarization of the virtual photon, E is the beam energy, p_A and θ_A are the central momentum and the angle of spectrometer A, p_{SOS} and θ_{SOS} are the central momentum and the angle of SOS.

ϵ	E (MeV)	p_A (MeV/ c)	θ_A ($^\circ$)	p_{SOS} (MeV/ c)	θ_{SOS} ($^\circ$)
0.902	855	656.2	22.5	82.7	44.5

The scattered electron in spectrometer A was detected in coincidence with the produced charged pion in the SOS. After the correction of the coincidence time for the particle path length in both spectrometers and adjustment of delays in electronics, a coincidence peak having a time resolution of 2.46 ns FWHM was obtained, see Fig. 10. The true electron-pion events were selected using a cut -2 ns $\leq T_{A-SOS} \leq 2.5$ ns. The contribution from random coincidence was estimated using data from the two sidebands: -52 ns $\leq T_{A-SOS} \leq -10$ ns and 6 ns $\leq T_{A-SOS} \leq 23$ ns.

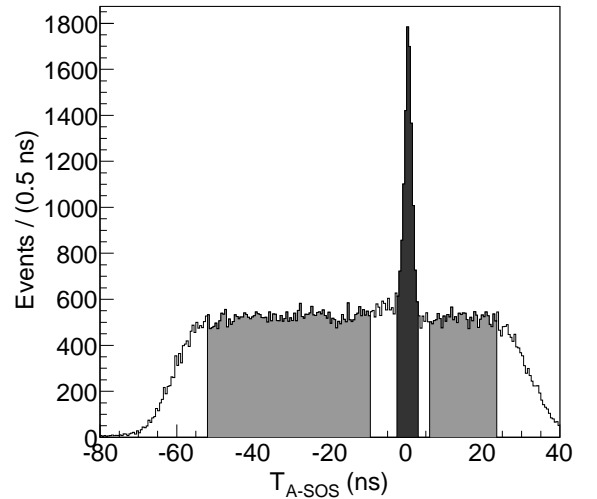


Figure 10: Coincidence time distribution. The dark gray area includes true coincidences and the light gray area contains only random coincidence events used for the background estimation.

Further reduction of background from random coincidences was achieved using additional cuts. Hence, a cut on the reconstructed electron momentum and a cut on the electron vertex reconstructed in spectrometer A were imposed. In case of the SOS, cuts were imposed on dispersive target coordinates and on energy deposited in the second and the third scintillator, which

were used to suppress the background from minimum ionizing particles, see Fig. 11.

As already observed in [9], when a particle passes very close to signal wires, the left-right decision can turn out wrong. Instead of the real trajectory, a trajectory having a wrong angle sign is reconstructed. This effect can easily be seen by plotting the dispersive SOS drift chamber coordinates x_{ch} vs. θ_{ch} , as shown in Fig. 12A. In order to correct for this issue the data stripes in lower right part of the distribution were isolated and their angle sign was changed intentionally [18]. Using this correction, the vacancies in the central distribution disappear (see Fig. 12B). Concurrently, the number of true events is raised by approximately 2%.

The effect of a wrong left-right decision is not unmistakably visible on the left hand side of the central distribution in Fig. 12 (both A and B). Either particles corresponding to the left part of the central distribution do not have trajectories for which the angle sign is easily reconstructed wrong, or the particles having a wrong angle sign are hidden in the central distribution. Nevertheless, if the latter would be the case the number of particles with wrong angle sign would still be very small.

4.1. Pion decay correction

The positive charged pions π^+ , on their path through the spectrometer, having a lifetime of $\tau_\pi = 26.033$ ns, may decay to a muon μ^+ and a muon neutrino ν_μ . The branching ratio for this decay channel is 99.9877% [5]. Decay can be described by:

$$\frac{N_\pi^{det}}{N_\pi^{tg}} = e^{-s/l_\pi} = \frac{1}{K_{decay}} \quad (10)$$

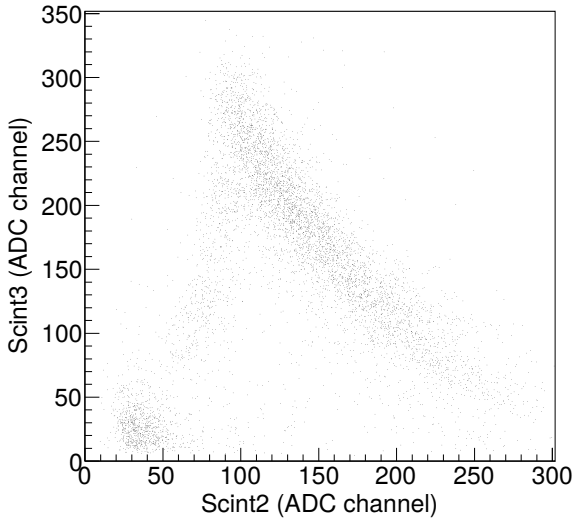


Figure 11: 2D distribution of deposited energy in the second vs. the third scintillator, obtained by using the cut on the coincidence peak and the fifth scintillator as a veto detector. Minimum ionizing particles are in the lower left corner of the figure and they are clearly separated from remaining particles. The rising and the falling slope correspond to pions which are stopped in the fourth and the third scintillator, respectively.

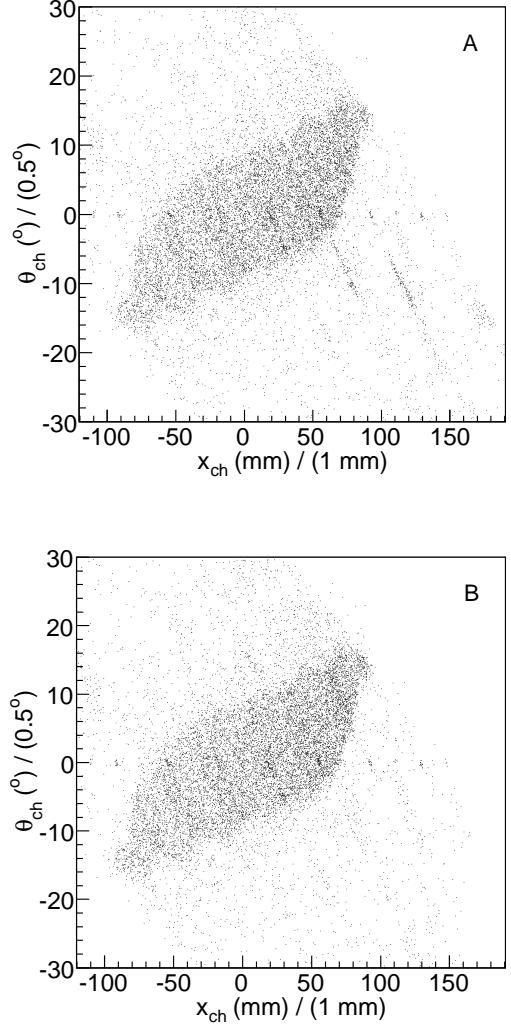


Figure 12: 2D distribution of dispersive SOS drift chamber coordinates x_{ch} vs. θ_{ch} . Figure A shows the distribution without left-right correction: the missing data can be clearly seen as empty stripes on the right hand side of central distribution. Since the angle of the missing data is reconstructed with a wrong sign, those data appear as stripes in the lower right corner of figure A. Figure B shows the data with left-right correction included: central distribution does not contain any empty stripes.

where N_π^{det} is the number of detected pions, N_π^{tg} is the number of created pions at the target, K_{decay} is the pion decay correction factor, s is the length of the pion path and l_π is the pion decay length, which can be calculated in the following way:

$$l_\pi = \gamma_\pi \tau_\pi \beta_\pi c = \tau_\pi c \left(\frac{p_\pi}{m_\pi c} \right) \quad (11)$$

The decay correction factor K_{decay} is calculated for each valid event. The calculation of the pion decay length l_π is straightforward by using equation (11), since the particle momentum p_π is measured by the spectrometer. The pion path length s is calculated using measured chamber coordinates, reconstructed target

coordinates and the known magnetic field of the SOS's dipole. A typical distribution of the K_{decay} can be seen in Fig. 13. The data in this figure show an average value of the pion decay correction factor of 1.45. From this we can estimate that 31% of pions produced at the target will decay before reaching the last detector.

4.2. Missing mass distribution

Using the reconstructed electron and pion four-momenta, the missing mass of an unobserved neutron was calculated for each electron-pion pair:

$$m_{miss} = \sqrt{(\omega + m_p - E_\pi)^2 - (\vec{q} - \vec{p}_\pi)^2} \quad (12)$$

where m_p is the proton mass, ω and \vec{q} are energy and momentum of the virtual photon, E_π and \vec{p}_π are energy and momentum of the pion. Since it is easier to notice possible deviations with respect to zero, the neutron mass m_n was subtracted from the calculated missing mass.

The background subtracted missing mass distribution of the measured kinematics can be seen in Fig. 14. As expected, the distribution shows a peak centered at bin zero, having an experimental width of 0.9 MeV/c² FWHM and a radiative tail on higher masses (see Fig. 14 inset).

5. Summary and conclusion

A new magnetic spectrometer – SOS – specialized for detection of low energy pions has been developed, built and successfully operated in electron scattering experiments at MAMI. Its detector system consists of volume type drift chambers and a 5-layer scintillator telescope.

The SOS has been calibrated using the $^{12}\text{C}(e, e'p)^{11}\text{B}$ reaction. Angular resolutions at the target were determined to be

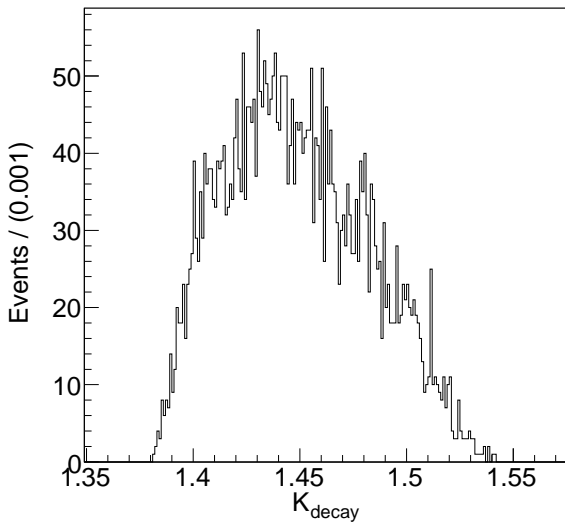


Figure 13: Distribution of the decay correction factors.

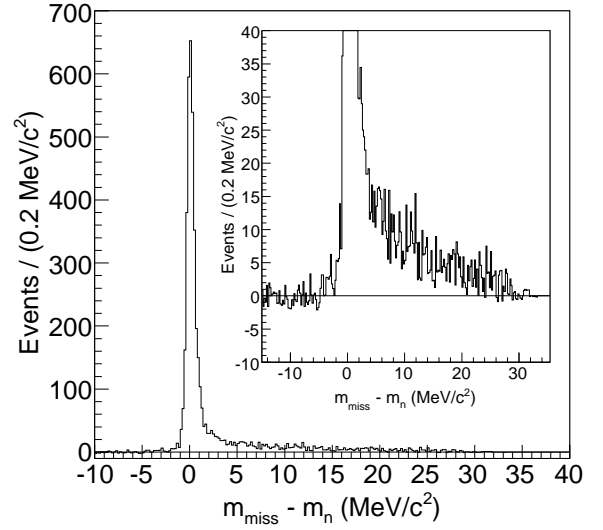


Figure 14: The missing mass distribution of the background subtracted data. The inset shows the radiative tail region of the same missing mass distribution.

$\sigma_{\theta_0} = 10.6$ mrad and $\sigma_{\phi_0} = 1.3$ mrad. The momentum resolution was estimated to be better than 1.3%.

The performance of the SOS to detect pions and measuring their momenta and energies was demonstrated in an electroproduction experiment with pions produced just 5 MeV above threshold.

The SOS is fully operable and can be used in high precision measurements involving low energy pions.

Acknowledgments

We would like to thank the MAMI accelerator group for the outstanding beam quality. This work was supported in part by the Deutsche Forschungsgemeinschaft with the Collaborative Research Centres 443 and 1044 and by the Croatian Science Foundation under project HRZZ 1680.

References

- [1] E. Amaldi, S. Fubini, G. Furlan, Pion Electroproduction, Vol. 83 of Springer Tracts in Modern Physics, Springer, Berlin, 1979. doi:10.1007/BFb0048208.
- [2] D. Drechsel, L. Tiator, J. Phys. G 18 (1992) 449. doi:10.1088/0954-3899/18/3/004.
- [3] K. I. Blomqvist, et al., Nucl. Instr. and Meth. Phys. Res. A 403 (1998) 263. doi:10.1016/S0168-9002(97)01133-9.
- [4] K.-H. Kaiser, et al., Nucl. Instr. and Meth. Phys. Res. A 593 (2008) 159. doi:10.1016/j.nima.2008.05.018.
- [5] J. Beringer, et al., Phys. Rev. D 86 (2012) 010001. doi:10.1103/PhysRevD.86.010001.
- [6] C. P. Browne, W. W. Buechner, Rev. Sci. Instr. 27 (1956) 899. doi:10.1063/1.1715411.
- [7] C. Schmitt, et al., Nucl. Instr. and Meth. Phys. Res. A 237 (1985) 523. doi:10.1016/0168-9002(85)91062-9.
- [8] D. Baumann, Ph.D. thesis, Johannes Gutenberg Univ. of Mainz (2005).
- [9] M. Ding, Ph.D. thesis, Johannes Gutenberg Univ. of Mainz (2004).
- [10] M. Ding, Diploma thesis, Johannes Gutenberg Univ. of Mainz (1997).

- [11] D. Baumann, Diploma thesis, Johannes Gutenberg Univ. of Mainz (1997).
- [12] S. Frullani, J. Mougey, Single Particle Properties of Nuclei through (e, e'p) Reactions, Vol. 14 of Advances in Nuclear Physics, Plenum Press, New York, 1984.
- [13] K. I. Blomqvist, et al., Z. Phys. A 351 (1995) 353. [doi:10.1007/BF01291135](https://doi.org/10.1007/BF01291135).
- [14] F. Ajzenberg-Selove, T. Lauritsen, Nucl. Phys. A 114 (1968) 1–142. [doi:10.1016/0375-9474\(68\)90820-8](https://doi.org/10.1016/0375-9474(68)90820-8).
- [15] M. Korn, Ph.D. thesis, Johannes Gutenberg Univ. of Mainz (1994).
- [16] S. Kowalsky, H. A. Enge, RAYTRACE, Technical Report No. 156, LNS-MIT, Cambridge MA, 1986.
- [17] S. Kowalsky, H. A. Enge, Nucl. Instr. and Meth. Phys. Res. A 258 (1987) 407. [doi:10.1016/0168-9002\(87\)90921-1](https://doi.org/10.1016/0168-9002(87)90921-1).
- [18] I. Friščić, Ph.D. thesis, Univ. of Zagreb (2015).